Geophysical Research Letters

RESEARCH LETTER
10.1002/2017GL076419

Key Points:
- We present exceptionally high amplitude infrasound recorded near a vulcanian eruption
- Infrasound analyses show the eruption onset as a 2-s vent failure including deformation and several pulses releasing 5×10^8 m^3 of gas
- Subsequent recordings reveal volcanic lightning and three distinct styles of emission

Supporting Information:
- Supporting Information S1

Correspondence to:
J. F. Anderson,
ajakef@gmail.com

Citation:
Anderson, J. F., Johnson, J. B., Steele, A. L., Ruiz, M. C., & Brand, B. D. (2018). Diverse eruptive activity revealed by acoustic and electromagnetic observations of the 14 July 2013 intense vulcanian eruption of Tungurahua volcano, Ecuador. *Geophysical Research Letters*, *45*. https://doi.org/10.1002/2017GL076419

Received 16 NOV 2017
Accepted 12 MAR 2018
Accepted article online 26 MAR 2018

Diverse Eruptive Activity Revealed by Acoustic and Electromagnetic Observations of the 14 July 2013 Intense Vulcanian Eruption of Tungurahua Volcano, Ecuador

J. F. Anderson[1], J. B. Johnson[1], A. L. Steele[2,3], M. C. Ruiz[2], and B. D. Brand[1]

[1]Department of Geosciences, Boise State University, Boise, ID, USA, [2]Instituto Geofisico, Escuela Politecnica Nacional, Quito, Ecuador, [3]UCL Hazard Centre, Department of Earth Sciences, University College London, London, UK

Abstract During the powerful July 2013 eruption of Tungurahua volcano, Ecuador, we recorded exceptionally high amplitude, long-period infrasound (1,600-Pa peak-to-peak amplitude, 5.5-s period) on sensors within 2 km of the vent alongside electromagnetic signals from volcanic lightning serendipitously captured as interference. This explosion was one of Tungurahua's most powerful vulcanian eruptions since recent activity began in 1999, and its acoustic wave is among the most powerful volcanic infrasound ever recorded anywhere. We use these data to quantify erupted volume from the main explosion and to classify postexplosive degassing into distinct emission styles. Additionally, we demonstrate a highly effective method of recording lightning-related electromagnetic signals alongside infrasound. Detailed chronologies of powerful vulcanian eruptions are rare; this study demonstrates that diverse eruptive processes can occur in such eruptions and that near-vent infrasound and electromagnetic data can elucidate them.

Plain Language Summary Vulcanian-type volcanic eruptions begin when pressurized gas in the vent is abruptly released in a powerful explosion. We recorded pressure waves produced in a powerful vulcanian-type eruption at Volcan Tungurahua (Ecuador) on 14 July 2013. The wave from the main explosion shows that the vent ruptured in a complex 2-s process including uplift followed by multiple distinct bursts, releasing an immense quantity of gas. This was among the most powerful pressure waves ever recorded from a vulcanian-type eruption. Subsequent waves show that the volcano continued to emit gas and ash after the main explosion; this emission occurred in three distinct types. Additionally, volcanic lightning was recorded serendipitously as interference in the acoustic data. Frequent lightning began abruptly 25 s after the eruption onset and became more sporadic 4 min later, finally ceasing 20 min after the explosion. This work shows that explosions and emissions in vulcanian eruptions can be complex and that acoustic recordings near the vent can elucidate these processes, strengthening volcano monitoring, and science.

1. Introduction

Infrasound is a valuable tool for all-weather monitoring of erupting volcanoes. Infrasound source processes can often be resolved in detail because path effects on infrasound near the vent are often small (Fee & Garces, 2007; Johnson & Lees, 2010) or predictable and straightforward to correct (Kim et al., 2015). Local infrasound is therefore useful in tracking the style (Fee & Matoza, 2013) and vigor (Gerst et al., 2013; Johnson & Miller, 2014) of eruptions. However, near-vent infrasound recording is most common at volcanoes with small, frequent eruptions; larger eruptions like the one in this study are typically recorded at longer distances (e.g., Fee et al., 2010). Longer-range recordings are useful, but waves are modified by path effects at such distances, making detailed inferences of volcanic activity more difficult (e.g., Green et al., 2012).

Several volcanic processes produce distinct types of infrasound. Some of the most energetic waves correspond to discrete vulcanian (Iguchi et al., 2008) and strombolian (Gerst et al., 2013) explosions, in which explosive gas release produces brief infrasound pulses a few seconds in duration that consist of a compression, rarefaction, and coda. The most powerful explosions generate nonlinear shock waves (Morrissey & Chouet, 1997) that decay into linear infrasound.

Other volcanic sources can generate continuous, long-duration infrasound tremor. For example, tremor from the vent can arise in gas jetting (Matoza et al., 2009; Steffke et al., 2010), streams of bubbles

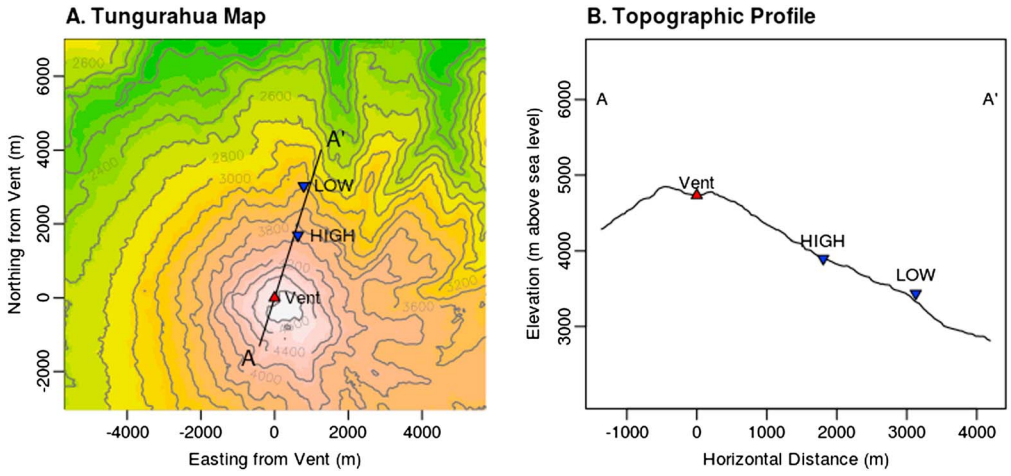

Figure 1. (a) Map of Tungurahua volcano and instrumentation network. (b) Topographic cross section including vent and sensors.

bursting at the lava surface (Ripepe et al., 2007; Ulivieri et al., 2013), and periodic series of emission pulses called chugging (Lees et al., 2008, 2004; Lees & Ruiz, 2008). Tremor also originates from pyroclastic density currents (PDCs) and lahars, which can be tracked with infrasound networks (Johnson & Palma, 2015; Ripepe et al., 2010; Yamasato, 1997).

Tungurahua was one of Ecuador's most active volcanoes from 1999 to 2016 and a prolific infrasound source. Its activity included strombolian, vulcanian, and subplinian explosions separated by intervals with weak or absent surface activity (Arellano et al., 2008; Hall et al., 2015). Tungurahua's infrasound included explosions, gas jetting, and chugging (Fee et al., 2010; Ruiz et al., 2006). The asymmetry of Tungurahua's crater and summit (Figure 1) focuses infrasound northwest and complicates recordings (Kim et al., 2012); these effects can be removed with numeric wave propagation modeling (Kim et al., 2015).

This paper examines a severe vulcanian eruption at Tungurahua at 11:47 UTC, 14 July 2013. The explosion's pressure wave was heard 180 km away, and its column reached 8.3 km above the crater. Falling lapilli damaged solar panels at least 6 km from the vent, and PDCs traveled 6.5 km from the vent (Instituto Geofisico, 2013). The vulcanian eruption was followed by occasional small explosions over the following 23 days (Narvaez, 2014). This was among Tungurahua's most powerful explosions since continuous, comprehensive geophysical monitoring began in 2006 and one of the most powerful vulcanian eruptions recorded with a nearby geophysical network anywhere in the world (Hall et al., 2015). We describe infrasound recordings of this violent eruption to elucidate its range of eruptive processes.

2. Field Data Collection

Our installation included two stations 1,860 m and 3,160 m north of the vent (Figure 1), each with three infrasonic microphones with flat responses above 0.01 Hz (Marcillo et al., 2012). Lab tests on these microphone types showed negligible nonlinearity at the excess pressures measured in this study. Infrasound was logged with a RefTek RT-130 data logger at station HIGH and a DataCube-3 at station LOW; the sample rate at these stations was 1000 and 100 Hz, respectively. Both data loggers recorded at 24 bit resolution with Global Positioning System timing. Sensor cables were shielded at station LOW but not at station HIGH, probably contributing to lightning-related electromagnetic interference in recordings from station HIGH (discussed in sections 3.3 and 4.4 and Text S2 in the supporting information).

Terrain and equipment constraints prevented the installation of triangular arrays, so linear arrays were deployed with ~15 m spacing between sensors. Although linear arrays cannot be used to calculate a unique back azimuth or incidence angle of incoming waves, the spatial separation of the array elements permits us to calculate coherence among sensors, a variable we consider when analyzing tremor (section 3.4).

3. Analysis

Infrasound analysis enables us to quantify eruptive activity by the amount of air it displaces (summarized in Table S1). We note that some of these analyses address details of waveforms that can be altered by path effects; therefore, recording infrasound near the vent where path effects are weak is essential.

Infrasonic pressure can be used to calculate erupted volume during discrete events. For linear acoustic waves emanating from an isotropic source, pressure recorded at the microphone corresponds to displaced air at the vent as

$$q(t) = H(t) * p(t) \tag{1}$$

where $q(t)$ is mass flow rate of displaced air, $H(t)$ is the inverse of the Green's function from the source to the receiver, "*" denotes convolution, and $p(t)$ is the infrasound time series in pressure units. When a signal is recorded at multiple sites with different Green's functions, an overdetermined linear system can be constructed and solved:

$$q_i = H_{ij} p_j, \tag{2}$$

where H_{ij} is the ordinary-least-squares generalized inverse of the Green's functions and p_j is the recorded data from all receivers (using the Einstein summation convention).

In the particular case when path effects (such as from topography, atmospheric heteogeneity, and attenuation) are negligible, equation (1) can be simplified as

$$q\left(t - \frac{r}{c}\right) = \Omega r \int_{t_1}^{t_2} p(t)\mathrm{d}t \tag{3}$$

where r is the distance between vent and microphone and Ω is the solid angle (about 9.08 sr at Tungurahua) subtended by the atmosphere around the vent (Lighthill, 1978). Otherwise, equation (2) must be used instead with Green's functions calculated using numeric models.

Equations (1)–(3) make four assumptions (Johnson, 2003). First, any instrument response, path or site effects, or radiation pattern anisotropy must be accounted for in H (and must be negligible if using equation (3)). We calculate Green's functions using finite-difference modeling with appropriate topography and atmospheric structure (Text S1 and Figures S1 and S2).

Second, long-period noise (such as from wind) and instrument drift (small trends in recordings not representative of actual pressure changes) must be negligible. Such noise is common in infrasound recordings and is problematic because trends and low frequencies are magnified by inversion, sometimes causing volume flow to be nonzero long after the end of the signal. Johnson and Miller (2014) solved this problem by estimating flow rate using equation (4) and detrending to make infrasound pressure and flow rate zero at the end of the signal. We use a slightly different detrending method because we use Green's functions from numeric models instead of equation (3). Using linear inversion, we find an optimal drift that minimizes the L2 norm of estimated flow rate:

$$q_i = H_{ij}\left(p_j - m t_j\right) \tag{4}$$

where m is the slope of the instrument drift and t_j is time (using the summation convention). Apart from instrument drift, signal-to-noise ratio is high during the explosion (Figure 2).

Third, the source dimensions must be small compared to acoustic wavelengths to justify a point source approximation. With vent dimensions of tens of meters compared to dominant wavelengths exceeding 1 km, this assumption is valid.

Fourth, pressure perturbations must be small relative to ambient pressure to justify the use of linear acoustic theory. This is easily satisfied for the precursory vent uplift but possibly not for the explosion. The wave from the explosion exceeded 1,200-Pa peak pressure at 2,158 m, so the wave's excess pressure probably reached 10% of ambient atmospheric pressure within 400 m of the vent. Nonlinear effects in this region could have caused waveform change and decay, which equations (1)–(4) cannot account for. However, significantly nonlinear propagation typically forms an abrupt signal onset, which we do not observe in this signal. Although we suggest that nonlinear effects on this wave were probably weak, we must consider our volume calculation to be conservative.

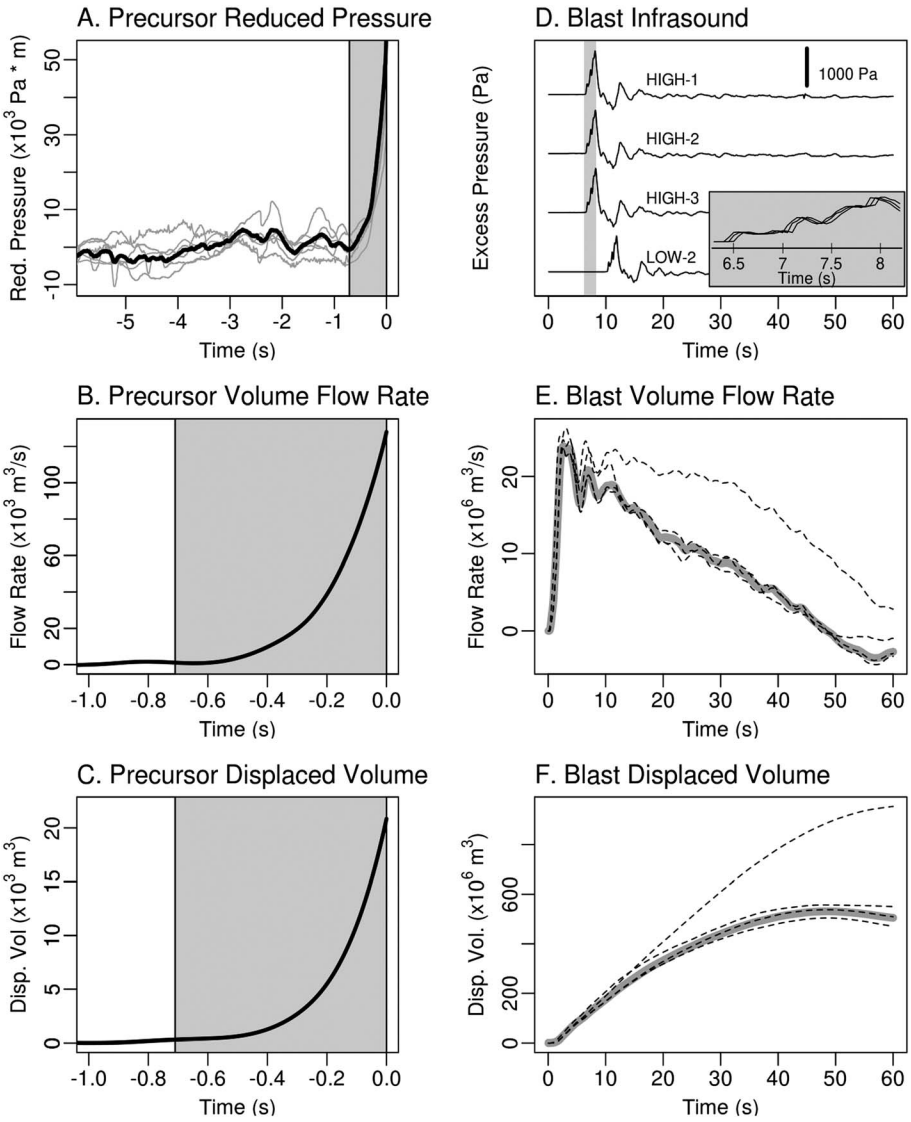

Figure 2. Infrasound and erupted volume inferences for the main explosion and precursory pulse. Times are relative to the explosion onset; traces are time shifted to vent to show stacking procedure in (a)–(c) but not in (d)–(f). (a) Reduced pressure of infrasound at all six stations (gray lines) and time-shifted stack (black). (b and c) Estimated instantaneous and cumulative volume flow. (d) Infrasound of main explosion. Inset: detail of stepped pressure rise. (e and f) Volume estimates from linear inversion with drift correction. Black dashed lines show single-station estimates of instantaneous volume flow rate. The highest single-station estimate (HIGH-3) is a clear outlier and is omitted from the multistation volume estimates (solid gray lines).

3.1. Main Vulcanian Blast

The eruption began abruptly with a major explosion that produced the high-amplitude infrasound signal (Figure 2). Like waves from many explosions, the waveform is dominated by a strong compression followed by a longer, weaker rarefaction (Morrissey & Chouet, 1997). However, unlike many explosion waveforms, the rise from ambient to peak pressure occurs in several distinct steps; pressure rises quickly at the onset of the waveform and 0.6, 1, and 1.4 s later (Figure 2).

Two of the three channels at station LOW clipped during the peak of the main blast arrival; consequently, data from those two microphones are excluded from the blast analysis. Only the main blast arrival was clipped in these two channels, so we did consider them in other analyses. The remaining channel at station LOW did not clip due to its lower sensitivity, and the high input voltage range of the RT-130 logger prevented clipping on any channel at station HIGH.

We apply equation (4) to quantify erupted volume using data from the four microphones that did not clip. We first estimate the volumetric eruption rate sensor by sensor and find that one sensor (HIGH-3) disagrees with the others (Figures 2e and 2f). This outlier is attributed to an uncorrected instrument drift or other long-period noise, and we omit it from subsequent calculations. The remaining three sensors agree closely with each other (±10% of cumulative flow). We invert these three records jointly for erupted volume, finding peak flow rate of 2.39×10^7 m^3/s and cumulative volume of 5.31×10^8 m^3.

3.2. Precursory Uplift

The first infrasound signal from this eruption was a relatively small emergent pressure increase (beginning at 11:46:38 UTC at the nearest station) that lasted about 0.71 s before being obscured by the main blast arrival (Figure 2). No coherent infrasound was recorded before the onset of the emergent pressure rise.

Inverting the brief, low-amplitude precursor using Green's functions from numeric models would be problematic because of possible acausal contamination from the blast wave. Instead, we invert the precursor using equation (3) (which is strictly causal) and correct for path effects by weighting each trace by the amplitude of the corresponding Green's function. Drift removal is performed by subtracting the trends found in the 14 s before the precursor began. Signal-to-noise ratio is not high during the precursor, so weighted traces are stacked to reduce noise.

We estimate the volume of displaced atmosphere during this uplift as 2.08×10^4 m^3 using equation (4) (Figure 2). Following interpretations of similar precursory pressure increases at Santiaguito (Johnson & Lees, 2010), Sakurajima (Yokoo et al., 2009), and Suwanosejima (Yokoo & Iguchi, 2010), we attribute this signal to vent surface uplift before gas escapes. The area of the vent that deformed during this phase is unknown, so we cannot calculate the height of the uplift.

3.3. Electrical Activity

Infrasound from station HIGH contains glitches (brief spikes in the time series) throughout the first 20 min of the eruption. Glitches do not appear at station LOW, possibly because of differences between the two loggers' locations, antialiasing filters, or cables (which were shielded at LOW but not at HIGH). These glitches include a one-sample voltage spike preceded and followed by brief oscillations (presumably induced by the data logger's antialiasing filter); they appear on all channels within the same sample interval (0.001 s) with distinct waveforms (Figure S3). Such characteristics are unlikely for acoustic waves but are typical of glitches observed to coincide with lightning strikes during thunderstorms, which are interpreted as electromagnetic interference from radio waves generated during lightning strikes (Anderson et al., 2014). Volcanic lightning is common in explosive eruptions and forms as a result of charging due to violent interactions between ash particles or, if present, hydrometeors (Behnke et al., 2013; Cimarelli et al., 2014).

Glitches are considered noise for the infrasound analysis and are therefore removed by a median filter before waveform inversion (Text S2). Although glitch elimination provides cleaned-up acoustic signals to analyze, we also analyze the timing of the glitches because they indicate lightning activity during the eruption. Lightning is absent from 0 to 25 s, frequent from 25 to 250 s, sparse from 250 to 1,250 s, and absent after 1,250 s (Figure 3). In total, we identify 119 lightning events, of which 93 occurred within 300 s of the explosion. For comparison, the World Wide Lightning Location Network (a network that detects lightning globally with low detection efficiency) detected three events, all of which appear in our data.

3.4. Tremor

The main vulcanian explosion is followed by a period of infrasonic tremor. We subdivide the tremor into types 1a, 1b, and 2 by waveform shape, amplitude, and semblance (Figure 3). The first tremor period (60–1,200 s) alternates between tremor 1a and 1b, and the second tremor period (1,200–3,000 s) consists of type 2 only. The following analyses are summarized in Table S2. All analyses are done with data from channel HIGH-2.

Waveform shape varies systematically during the long period of tremor following the explosion, with some periods composed of strongly asymmetric pulses (higher-amplitude compressions than rarefactions) and other periods fluctuating more evenly about 0. To quantify pulse asymmetry over long

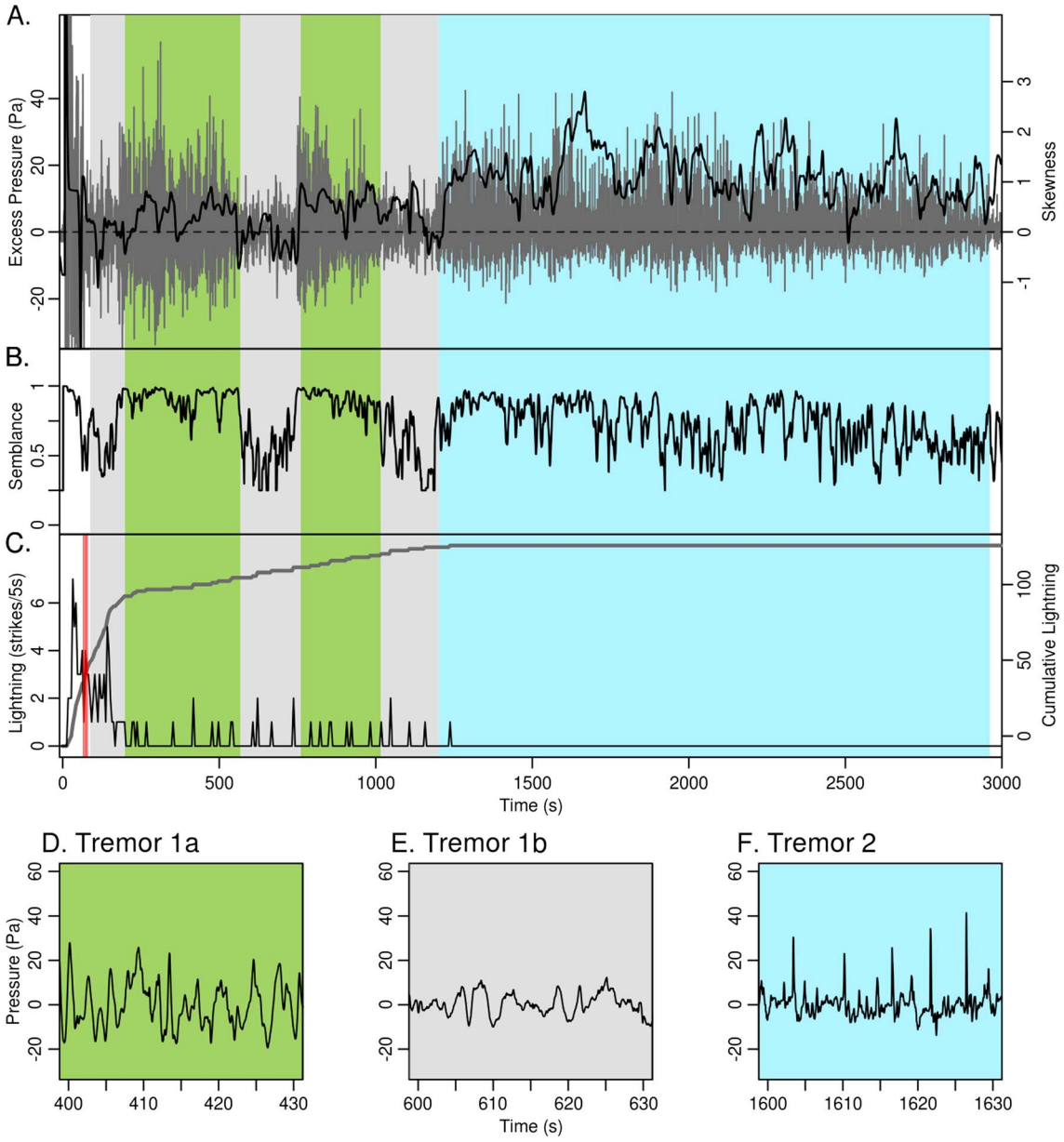

Figure 3. (a) Acoustic waveforms (gray) and skewness (black). (b) Semblance. (c) Lightning occurrence as binned event counts (black) and cumulative counts (gray). Red line represents World Wide Lightning Location Network detections (three events detected, all within 11 s). Background color shows tremor type. (d–f) Examples of tremor types 1a, 1b, and 2. Tremor types are distinguished in time series by their differing amplitude, semblance, and waveform shape.

timescales, we plot Pearson's moment coefficient for skewness for moving 50-s windows. Skewness is defined as

$$\widetilde{\mu_3} = \frac{1}{N}\sum_{i=1}^{N}\left(\frac{p_i - \mu}{\sigma}\right)^3$$

where $\widetilde{\mu_3}$ is skewness, μ is the mean, σ is standard deviation, and N is the number of samples in a window. This measure quantifies the degree to which tremor is dominated by strongly asymmetric pulses (Fee et al., 2013).

Additionally, we calculate semblance as an indicator of wave coherence. For a window of n samples, the semblance S is defined as

$$S = \frac{\sum_{i=1}^{n}\left[\sum_{j=1}^{3} p_j\left(t_i - \delta t_j\right)\right]^2}{3\times\sum_{i=1}^{n}\sum_{j=1}^{3} p_j\left(t_i - \delta t_j\right)^2},$$

where p_j is the infrasound recorded at microphone j, t_i is the time step i, and δt_j is the time shift at microphone

j for the apparent velocity. For each window, we test a range of apparent velocities and use the maximum semblance value obtained.

Tremors 1a and 1b both feature continuous, stationary waveforms. However, they differ from each other in skewness, amplitude, and semblance. Skewness of tremor 1b fluctuates around 0, while tremor 1a ranges from about 0 to 1. Further, both semblance and amplitude are greater in tremor 1a than tremor 1b.

Tremor 2 differs from tremors 1a and 1b mainly by waveform shape. Unlike the continuous waveforms of tremors 1a and 1b, tremor 2 waveforms consist of closely spaced asymmetric pulses separated by irregular time intervals. Each pulse includes a strong, short-duration compression followed by a weak, longer-duration rarefaction; amplitudes of compressions are 2–3 times those of rarefactions. Correspondingly, skewness rises sharply at the onset of type 2 tremor and remains high throughout that period, demonstrating that the visible differences in waveform shape constitute a large-scale structural difference between these tremor types. Zero-to-peak amplitudes of tremor 2 are similar to those of tremor 1a, but peak-to-peak and root-mean-square amplitudes are lower in tremor 2; this discrepancy results from the high skewness of tremor 2.

4. Discussion

We divide the volcano's activity into three periods, including the main vulcanian explosion and two distinct degassing phases.

4.1. Main Vulcanian Explosion

Before the explosion, the vent was sealed and contained a large quantity of pressurized gas. Surface activity began with a rapid uplift of the vent, creating a precursory acoustic pulse lasting at least 0.71 s and displacing at least 20,800 m^3 of air. Because the shock wave produced by gas release may have propagated supersonically and partially overrun this precursor, the uplift might be underestimated.

Explosive gas and tephra ejection followed the vent uplift. The stepped rise of the wave onset in the infrasound data (Figure 2) suggests that gas release occurred in pulses, probably due to incremental opening of the conduit or successive tapping of deeper gas-charged sections of the magma column. Altogether, the total erupted volume from the main explosion is estimated as 5.31×10^8 m^3 including gas and tephra (Fee et al., 2017). If, contrary to our assumptions, nonlinear propagation effects were significant, these values would be underestimates.

To provide context for the scale of the 14 July 2013 eruption, we compare it to the two largest explosions from a recent period of explosive activity at Sakurajima volcano, Japan (explosions 3 and 5 of Johnson & Miller, 2014). Infrasound analysis indicated that the 2013 Sakurajima explosions erupted 8.3 and 8.4×10^6 m^3 of volcanic gas and tephra, a factor of 63 less than the volume erupted at Tungurahua. Compared to these eruptions, Tungurahua's blast wave had a longer compression duration (2.4 s compared to about 1 s at Sakurajima) and a higher peak-to-peak reduced amplitude (3.4×10^6 Pa · m compared to 3.9×10^5 and 7.4×10^5 Pa · m at Sakurajima). Therefore, the Tungurahua explosion was considerably larger than these Sakurajima explosions by several measures, especially by infrasound-inferred erupted volume. By infrasound amplitude, this explosion was also more powerful than any other discrete explosion at Tungurahua since the current monitoring network was installed in 2006. In particular, the peak-to-peak amplitude of the July 2013 explosion exceeds amplitudes of later vulcanian eruptions in October 2013 and February 2014 by factors of 1.7 and 2.9, respectively (Hall et al., 2015).

In this explosion, the vent opened in a complex ~2-s process including preexplosive vent deformation and a series of emission pulses. Similar multipulse superposition of blasts is evident, though less pronounced, in explosions at Sakurajima (Fee et al., 2014; Johnson & Miller, 2014), and similar preexplosive deformation has been observed at volcanoes including Sakurajima (Yokoo et al., 2009) and Suwanosejima (Yokoo & Iguchi, 2010). These observations demonstrate the complexity of vent processes that can initiate powerful explosions: vent opening can be a series of events rather than one single failure. By comparison, the explosive mechanism was much simpler (single explosive pulse, no preexplosive deformation) in Tungurahua's small explosions in the weeks following 14 July 2013.

4.2. Continuous Tephra-Rich Degassing

Infrasonic tremor oscillating between types 1a and 1b follows the explosion and is accompanied by sporadic electrical discharge. The lack of discrete waveforms within the tremor indicates a relatively continuous emission process, although the variation in amplitude between these tremor types shows that emission vigor fluctuated over timescales of tens to hundreds of seconds.

During tremor 1a periods, the high semblance among sensors corresponds to high signal-to-noise ratio and a single dominant acoustic source. As a result, we consider this signal to indicate continuous magma fragmentation at the vent, either by downward propagation of a fragmentation wave (Alidibirov, 1994) or continuous ascent and bursting of bubbles (Ulivieri et al., 2013).

We interpret the low-semblance signals of tremor 1b to be dominated by incoherent pressure variations that mask eruptive signals during periods of reduced emission vigor. This incoherence probably arises from severe wind noise, possibly driven by updrafts near the vent, as station HIGH was installed in a sparsely vegetated site with no wind reduction system. Other possible sources of incoherent noise may include PDCs that passed within hundreds of meters of station HIGH (Hall et al., 2015) and falling ejecta.

Electrical discharge began before the first tremor period and continued throughout. The incidence of lightning-linked glitches agrees with the pattern seen in recent studies at Augustine (Thomas et al., 2007), Redoubt (Behnke et al., 2013), and Eyjafjallajökull volcanoes (Behnke & McNutt, 2014). These studies describe explosive eruptions in which electrical discharge started near the vent soon after explosive activity began. Two styles of discharge occur during this period: vent discharge (small events occurring continuously at the vent) and near-vent lightning (higher-power discrete lightning flashes near the vent). A third type of discharge, referred to as plume lightning, occurs when a plume is present; plume lightning occurs in long, powerful, discrete flashes similar to thunderstorm lightning (Behnke et al., 2013).

Similarly, we observe a period between about 25 and 250 s after the eruption onset with frequent discharges (around several tens of discharges per minute). The beginning of this phase is abrupt, and no discharges are observed earlier. These discharges are probably near-vent lightning; our instrumentation is not designed for sensitivity to electrical activity and is therefore unlikely to record the lower-power vent discharge. After about 250 s, electrical discharge becomes much less frequent (around 1–2 discharges per minute). Because we cannot locate these events, we cannot classify them between plume lightning and near-vent lightning. The period of sparse lightning ends around 1,250 s, and no further discharges occur after that time.

4.3. Pulsed Degassing

The properties of the tremor signal change abruptly around 1,200 s. This new signal, labeled tremor 2, is dominated by discrete pulses separated by irregular time intervals. Pulsed degassing continues for 1,800 s before diminishing.

Electrical discharge also ceases around the beginning of the pulsed degassing phase. Two interpretations of plume activity could explain the absence of discharges. The first possibility is that plume electrification was driven by volcanic emissions during the first tremor period, so lightning diminished when the style of emission changed. The second possibility is that plume electrification resulted from an initial intense venting of gas and ash—not by emissions during the first tremor period—and that by coincidence the plume electrical activity stopped around the transition to tremor 2. In either case, emission during the tremor 2 period was insufficient to create a column or cloud with electrical activity.

We consider two potential sources for tremor 2, one being small, repeated bursts at the vent. This mechanism is suggested by the resemblance between these pulses and explosion waveforms (sharp, brief compressions followed by longer, weaker rarefactions). These events could be bubbles ascending to the magma surface and bursting (e.g., Ulivieri et al., 2013) or cycles in which permeable crack networks in the magma pressurize, burst, and reseal.

These waveforms also resemble "crackle," a type of signal produced by supersonic jetting. Waveforms similar to tremor 2 were recorded at regional distances during the June 2011 eruption of Nabro volcano (Eritrea) and Stromboli volcano (Italy) and were attributed to supersonic gas jetting because of their similarity to noise from rocket and jet engines (Fee et al., 2013; Goto et al., 2014). Crackle was associated with the remarkably

ash-poor, gas-rich character of the Nabro and Stromboli emissions. We speculate that ash-poor jetting could potentially explain both the absence of electrical activity and this tremor.

4.4. Recording Volcanic Lightning Alongside Infrasound

Our method of lightning glitch logging—connecting infrasound microphones to a data logger with long unshielded cables—was discovered by accident in this campaign but will be useful in future infrasound projects. If a local infrasound station is already being installed, this method yields lightning event times with no additional equipment, expense, or installation time, and minimal extra data processing, and with higher detection efficiency than is possible with global networks like World Wide Lightning Location Network. The timing and event frequency of volcanic lightning—which is driven by conditions in the plume—can therefore serve as an easily obtained but valuable complement to existing monitoring data (which typically offer little information on plume conditions in cloudy weather).

However, this method has downsides and is inappropriate in some scenarios. For example, if more detailed information (like discharge location and power) is required, the method in this paper is insufficient and a dedicated lightning monitoring system should be used (Behnke & McNutt, 2014). Additionally, because the median filter acts as a low-pass filter on ordinary data, a higher sample rate than normal may be needed to prevent the median filter from attenuating high acoustic frequencies of interest.

5. Conclusion

We analyzed near-vent infrasound data from the 14 July 2013 vulcanian eruption at Tungurahua in order to quantify explosion dynamics and describe subsequent eruptive activity. Ash and gas can be released by diverse and complex processes in powerful vulcanian eruptions, and near-vent infrasound and electromagnetic data can differentiate these processes. Lightning-related glitches in the infrasound record indicate that volcanic lightning began abruptly 25 s after the eruption onset and diminished over the next 20 min; future infrasound projects could easily record lightning using our method with little effort and no extra equipment.

The eruption began with the opening of a sealed magma conduit containing pressurized exsolved gas. A complex failure process including vent uplift and a series of gas emission pulses opened the vent over a 2-s period, resulting in the rapid expulsion of at least 5×10^8 m^3 of gas and tephra. Volcanic lightning (registered as glitches in acoustic data) began 25 s after the explosion. Continuous fragmentation in the conduit emitted ash and gas and produced continuous infrasonic tremor starting 50 s after the explosion and lasting about 1,150 s. Finally, electrical activity in the plume ceased; simultaneously, vent activity transitioned to either pulsed degassing or supersonic ash-poor gas jetting, producing pulsed infrasonic tremor lasting 1,800 s.

Acknowledgments
We thank J. Anzieta, J. Cordoba, D. Litchfield, and H. Ortiz for field assistance, J. Lees for providing instruments, and Instituto Geofisico-Escuela Politecnica Nacional for logistical support. NSF grant EAR-0838562 funded this work. Infrasound data are archived at IRIS DMC (https://doi.org/10.7914/SN/8A_2013). WWLLN data are available from http://wwlln.net. We thank R. Matoza and D. Fee for helpful reviews.

References

Alidibirov, M. A. (1994). A model for viscous magma fragmentation during volcanic blasts. *Bulletin of Volcanology*, *56*(6-7), 459–465. https://doi.org/10.1007/BF00302827

Anderson, J. F., Johnson, J. B., Arechiga, R. O., & Thomas, R. J. (2014). Mapping thunder sources by inverting acoustic and electromagnetic observations. *Journal of Geophysical Research: Atmospheres*, *119*, 287–304. https://doi.org/10.1002/2014JD021624

Arellano, S. R., Hall, M., Samaniego, P., Le Pennec, J.-L., Ruiz, A., Molina, I., & Yepes, H. (2008). Degassing patterns of Tungurahua volcano (Ecuador) during the 1999–2006 eruptive period, inferred from remote spectroscopic measurements of SO_2 emissions. *Journal of Volcanology and Geothermal Research*, *176*(1), 151–162. https://doi.org/10.1016/j.jvolgeores.2008.07.007

Behnke, S. A., & McNutt, S. R. (2014). Using lightning observations as a volcanic eruption monitoring tool. *Bulletin of Volcanology*, *76*(8), 1–12.

Behnke, S. A., Thomas, R. J., McNutt, S. R., Schneider, D. J., Krehbiel, P. R., Rison, W., & Edens, H. E. (2013). Observations of volcanic lightning during the 2009 eruption of Redoubt Volcano. *Journal of Volcanology and Geothermal Research*, *259*, 214–234. https://doi.org/10.1016/j.jvolgeores.2011.12.010

Cimarelli, C., Alatorre-Ibargüengoitia, M. A., Kueppers, U., Scheu, B., & Dingwell, D. B. (2014). Experimental generation of volcanic lightning. *Geology*, *42*(1), 79–82. https://doi.org/10.1130/G34802.1

Fee, D., & Garces, M. (2007). Infrasonic tremor in the diffraction zone. *Geophysical Research Letters*, *34*, L16826. https://doi.org/10.1029/2007GL030616

Fee, D., Garces, M., & Steffke, A. (2010). Infrasound from Tungurahua Volcano 2006-2008: Strombolian to Plinian eruptive activity. *Journal of Volcanology and Geothermal Research*, *193*(1-2), 67–81. https://doi.org/10.1016/j.jvolgeores.2010.03.006

Fee, D., Izbekov, P., Kim, K., Yokoo, A., Lopez, T., Prata, F., et al. (2017). Eruption mass estimation using infrasound waveform inversion and ash and gas measurements: Evaluation at Sakurajima Volcano, Japan. *Earth and Planetary Science Letters*, *480*, 42–52. https://doi.org/10.1016/j.epsl.2017.09.043

Fee, D., & Matoza, R. S. (2013). An overview of volcano infrasound: From Hawaiian to Plinian, local to global. *Journal of Volcanology and Geothermal Research*, *249*, 123–139. https://doi.org/10.1016/j.jvolgeores.2012.09.002

Fee, D., Matoza, R. S., Gee, K. L., Neilsen, T. B., & Ogden, D. E. (2013). Infrasonic crackle and supersonic jet noise from the eruption of Nabro Volcano, Eritrea. *Geophysical Research Letters*, *40*, 4199–4203. https://doi.org/10.1002/grl.50827

Fee, D., Yokoo, A., & Johnson, J. B. (2014). Introduction to an open community infrasound dataset from the actively erupting Sakurajima Volcano, Japan. *Seismological Research Letters*, *85*(6), 1151–1162. https://doi.org/10.1785/0220140051

Gerst, A., Hort, M., Aster, R. C., Johnson, J. B., & Kyle, P. R. (2013). The first second of volcanic eruptions from the Erebus volcano lava lake, Antarctica—Energies, pressures, seismology, and infrasound. *Journal of Geophysical Research: Solid Earth*, *118*, 3318–3340. https://doi.org/10.1002/jgrb.50234

Goto, A., Ripepe, M., & Lacanna, G. (2014). Wideband acoustic records of explosive volcanic eruptions at Stromboli: New insights on the explosive process and the acoustic source. *Geophysical Research Letters*, *41*, 3851–3857. https://doi.org/10.1002/2014GL060143

Green, D. N., Matoza, R. S., Vergoz, J., & Le Pichon, A. (2012). Infrasonic propagation from the 2010 Eyjafjallajökull eruption: Investigating the influence of stratospheric solar tides. *Journal of Geophysical Research*, *117*, D21202. https://doi.org/10.1029/2012JD017988

Hall, M. L., Steele, A. L., Bernard, B., Mothes, P. A., Vallejo, S. X., Douillet, G. A., et al. (2015). Sequential plug formation, disintegration by vulcanian explosions, and the generation of granular pyroclastic density currents at Tungurahua volcano (2013–2014), Ecuador. *Journal of Volcanology and Geothermal Research*, *306*, 90–103. https://doi.org/10.1016/j.jvolgeores.2015.09.009

Iguchi, M., Yakiwara, H., Tameguri, T., Hendrasato, H., & Hirabayashi, J. (2008). Mechanism of explosive eruption revealed by geophysical observations at the Sakurajima, Suwanosejima, and Semeru volcanoes. *Journal of Volcanology and Geothermal Research*, *178*(1), 1–9. https://doi.org/10.1016/j.jvolgeores.2007.10.010

Instituto Geofisico (2013). Informe especial del Volcan Tungurahua No. 15. Retrieved from http://www.igepn.edu.ec/tungurahua/informes-tungurahua/tung-especiales/tung-e-2013/8920-informe-especial-no-15-16julio/file

Johnson, J. B. (2003). Generation and propagation of infrasonic airwaves from volcanic explosions. *Journal of Volcanology and Geothermal Research*, *121*(1-2), 1–14. https://doi.org/10.1016/S0377-0273(02)00408-0

Johnson, J. B., & Lees, J. M. (2010). Sound produced by the rapidly inflating Santiaguito lava dome, Guatemala. *Geophysical Research Letters*, *37*, L22305. https://doi.org/10.1029/2010GL045217

Johnson, J. B., & Miller, A. J. C. (2014). Application of the monopole source to quantify explosive flux during vulcanian explosions at Sakurajima volcano (Japan). *Seismological Research Letters*, *35*, 1163–1176.

Johnson, J. B., & Palma, J. L. (2015). Lahar infrasound associated with Volcan Villarrica's 3 March 2015 eruption. *Geophysical Research Letters*, *42*, 6324–6331. https://doi.org/10.1002/2015GL065024

Kalnay, E., Kanamitsu, M., & Baker, W. E. (1990). Global numerical weather prediction at the National Meteorological Center. *American Meteorological Society*, *71*(10), 1410–1428. https://doi.org/10.1175/1520-0477(1990)071%3C1410:GNWPAT%3E2.0.CO;2

Kim, K., Fee, D., Yokoo, A., & Lees, J. M. (2015). Acoustic source inversion to estimate volume flux from volcanic explosions. *Geophysical Research Letters*, *42*, 5243–5249. https://doi.org/10.1002/2015GL064466

Kim, K., Lees, J. M., & Ruiz, M. (2012). Acoustic multipole source model for volcanic explosions and inversion for source parameters. *Geophysical Journal International*, *191*(3), 1192–1204. https://doi.org/10.1111/j.1365-246X.2012.05696.x

Lees, J. M., Gordeev, E. I., & Ripepe, M. (2004). Explosions and periodic tremor at Karymsky volcano, Kamchatka, Russia. *Geophysical Journal International*, *158*(3), 1151–1167. https://doi.org/10.1111/j.1365-246X.2004.02239.x

Lees, J. M., Johnson, J. B., Ruiz, M., Troncoso, L., & Welsh, M. (2008). Reventador volcano 2005: Eruptive activity inferred from seismo-acoustic observation. *Journal of Volcanology and Geothermal Research*, *176*(1), 179–190. https://doi.org/10.1016/j.jvolgeores.2007.10.006

Lees, J. M., & Ruiz, M. (2008). Non-linear explosion tremor at Sangay volcano, Ecuador. *Journal of Volcanology and Geothermal Research*, *176*(1), 170–178. https://doi.org/10.1016/j.jvolgeores.2007.08.012

Lighthill, M. J. (1978). *Waves in fluids*. New York: Cambridge University Press.

Marcillo, O., Johnson, J. B., & Hart, D. (2012). Implementation, characterization, and evaluation of an inexpensive low-power low-noise infrasound sensor based on a micromachined differential pressure transducer and a mechanical filter. *Journal of Atmospheric and Oceanic Technology*, *29*(9), 1275–1284. https://doi.org/10.1175/JTECH-D-11-00101.1

Matoza, R. S., Fee, D., Garces, M. A., Seiner, J. M., Ramon, P. A., & Hedlin, M. A. H. (2009). Infrasonic jet noise from volcanic eruptions. *Geophysical Research Letters*, *36*, L08303. https://doi.org/10.1029/2008GL036486

Morrissey, M. M., & Chouet, B. A. (1997). Burst conditions of explosive volcanic eruptions recorded on microbarographs. *Science*, *275*(5304), 1290–1293. https://doi.org/10.1126/science.275.5304.1290

Narvaez, D. (2014). Caracterizacion de los dinamismos eruptivos de los periodos de actividad de marzo y julio del volcan Tungurahua, con base en el estudio morfo-granulometrico, geoquimico y modal de los productos de caida, (Master's thesis). Escuela Politecnica Nacional, Quito, Ecuador.

NASA/METI/AIST/Japan Spacesystems, and U.S./Japan ASTER Science Team (2009). ASTER global digital elevation model [data set]. NASA EOSDIS Land Processes DAAC. https://doi.org/10.5067/ASTER/ASTGTM.002

Ripepe, M., De Angelis, S., Lacanna, G., & Voight, B. (2010). Observation of infrasonic and gravity waves at Soufriere Hills Volcano, Montserrat. *Geophysical Research Letters*, *37*, L00E14. https://doi.org/10.1029/2010GL042557

Ripepe, M., Marchetti, E., & Ulivieri, G. (2007). Infrasonic monitoring at stromboli volcano during the 2003 effusive eruption: Insights on the explosive and degassing process of an open conduit system. *Journal of Geophysical Research*, *112*, B09207. https://doi.org/10.1029/2006JB004613

Ruiz, M. C., Lees, J. M., & Johnson, J. B. (2006). Source constraints of Tungurahua volcano explosion events. *Bulletin of Volcanology*, *68*(5), 480–490. https://doi.org/10.1007/s00445-005-0023-8

Steffke, A. M., Fee, D., Garces, M., & Harris, A. (2010). Eruption chronologies, plume heights and eruption styles at Tungurahua Volcano: Integrating remote sensing techniques and infrasound. *Journal of Volcanology and Geothermal Research*, *193*(3-4), 143–160. https://doi.org/10.1016/j.jvolgeores.2010.03.004

Thomas, R. J., Krehbiel, P. R., Rison, W., Edens, H. E., Aulich, G. D., Winn, W. P., et al. (2007). Electrical activity during the 2006 Mount St. Augustine volcanic eruptions. *Science*, *315*(5815), 1097.

Ulivieri, G., Ripepe, M., & Marchetti, E. (2013). Infrasound reveals transition to oscillatory discharge regime during lava fountaining: Implication for early warning. *Geophysical Research Letters*, *40*, 3008–3013. https://doi.org/10.1002/grl.50592

Yamasato, H. (1997). Quantitative analysis of pyroclastic flows using infrasonic and seismic data at Unzen volcano, Japan. *Journal of Physics of the Earth*, *45*, 397–416.

Yokoo, A., & Iguchi, M. (2010). Using infrasound waves from eruption video to explain ground deformation preceding the eruption of Suwanosejima volcano, Japan. *Journal of Volcanology and Geothermal Research*, *196*(3-4), 287–294. https://doi.org/10.1016/j.jvolgeores.2010.08.008

Yokoo, A., Tameguri, T., & Iguchi, M. (2009). Swelling of a lava plug associated with a vulcanian eruption at Sakurajima Volcano, Japan, as revealed by infrasound record: Case study of the eruption on January 2, 2007. *Bulletin of Volcanology*, *71*(6), 619–630. https://doi.org/10.1007/s00445-008-0247-5